Journal of
Materials Chemistry B

ROYAL SOCIETY
OF CHEMISTRY

PAPER

View Article Online
View Journal | View Issue

Cite this: *J. Mater. Chem. B*, 2025, **13**, 3460

Room temperature operated flexible MWCNTs/Nb_2O_5 hybrid breath sensor for the non-invasive detection of an exhaled diabetes biomarker†

Gulshan Verma,[a] Sonu Sarraf,[b] Aviru K. Basu,[b] Pranay Ranjan[c] and Ankur Gupta *[a]

Received 27th November 2024,
Accepted 4th February 2025

DOI: 10.1039/d4tb02644f

rsc.li/materials-b

Advancements in diabetes management increasingly rely on non-invasive monitoring of biomarkers present in exhaled breath. This study introduces a novel room temperature operated flexible acetone sensing platform, leveraging a hybrid material composed of multi-walled carbon nanotubes (MWCNTs) and niobium oxide (Nb_2O_5). The platform demonstrates sensitivity and selectivity towards acetone, a prominent biomarker of diabetes, offering promise for real-time health monitoring applications. The sensor exhibited a characteristic feature of fast response (25 s) and recovery times (46 s) at 50 ppm, good selectivity, and stability with a detection limit of 330 ppb. Additionally, the sensor's characteristic features were collected, and four different machine learning (ML) algorithms were applied to visualize and classify the gases with good quantification. Out of all algorithms, the random forest (RF) algorithm demonstrates the best performance. Furthermore, regression modelling was also used to quantitatively predict the gas concentration. In addition, the sensor was shown to distinguish between signals from simulated diabetic and healthy breath samples. These sensing performances indicate that the breath sensor has practical applications that could potentially provide a non-invasive monitoring method for diabetic patients.

1. Introduction

Diabetes mellitus, a chronic metabolic disorder characterized by elevated blood glucose levels, poses significant challenges to global public health. Effective management of diabetes relies heavily on continuous monitoring of blood glucose levels, traditionally achieved through invasive methods such as finger-stick testing. However, the pursuit of non-invasive monitoring approaches has gained attraction due to their potential to enhance patient compliance and quality of life. Among emerging non-invasive techniques, the analysis of exhaled breath biomarkers presents a promising avenue for real-time monitoring and early detection of diabetes-related metabolic changes. Gas sensors can be a potential solution to this problem and can play a crucial role in modern advanced devices, allowing swift monitoring, detection, and regulation of gas mixtures and vapors in the surrounding environment.[1,2] Among the gases, acetone, a common volatile organic compound (VOC), is widely used in industry, households, medicine, and various other fields.[3] However, owing to its high volatility, acetone inhalation poses significant health risks.[4] Even at concentrations of several hundred parts per million (ppm), it can lead to headaches, respiratory issues, dizziness, and other adverse effects.[5] The rapid detection and precise measurement of ultralow concentrations of acetone vapor (ranging from 0.7 to 5 ppm) play a pivotal role in designing cutting-edge medical diagnostic systems.[6] Analyzing human exhaled breath offers a non-invasive approach to detecting and investigating specific diseases. Notably, even minor fluctuations in acetone levels within the exhaled breath can signal the presence of diabetes. Furthermore, acetone is a crucial raw material for organic synthesis in modern industrial processes; however, high concentrations of acetone can pose risks in the workplace, including explosive accidents and irreversible damage to humans. To address this critical need, the development of highly selective, rapid, and sensitive acetone detectors with nanoscale structures is essential.[7] Furthermore, wearable flexible acetone sensors provide continuous, real-time monitoring of acetone concentrations. Their flexibility ensures wear comfort and unobtrusiveness, making them suitable for medical diagnostics and environmental safety applications.

---

[a] *Department of Mechanical Engineering, Indian Institute of Technology Jodhpur, Jodhpur, Rajasthan, 342030, India. E-mail: ankurgupta@iitj.ac.in*
[b] *Quantum Materials and Devices Unit, Institute of Nano Science and Technology, Mohali, Punjab, 140306, India*
[c] *Department of Material and Metallurgical Engineering, Indian Institute of Technology Jodhpur, Jodhpur, Rajasthan, 342030, India*

† Electronic supplementary information (ESI) available. See DOI: **https://doi.org/10.1039/d4tb02644f**

The sensitivity and reliability of gas sensors are enhanced by the interactions between the gas molecules and the sensing material, which are influenced by the available active surface area.[8] This can further enhance the specificity of the sensor, allowing it to distinguish between different gas types based on their chemical properties. Numerous reports have discussed the sensing performance of nanostructured metal oxides (MO_x),[9] yet relatively few studies have explored the feasibility of transition MO_x, such as Nb_2O_5, for gas/breath sensing. Nb_2O_5, a wide bandgap n-type metal oxide, has desirable properties such as excellent chemical stability, low film stress, and a high refractive index (n = 2.4 at 550 nm).[10] The intercalation reactions of Nb_2O_5 are highly sensitive to the preparation temperature and particle size. Nb_2O_5 exhibits various polymorphic forms depending on the preparation temperature,[11] including orthorhombic, tetragonal, pseudo-hexagonal, and monoclinic phases. Owing to its remarkable properties, Nb_2O_5 is utilized in a range of applications, such as catalysis, batteries,[12] solar cells,[13] and optical sensors.[14] Several synthesis methods have been reported to obtain nanostructured Nb_2O_5, including sol–gel dip-coatings,[15] hydrothermal,[16] and electrodeposition.[17] Recently, researchers have focused on the preparation of Nb_2O_5 nanostructures for sensing applications. Moreover, Nb_2O_5 nanowire arrays show moderate sensing performance of the prepared hydrogen sensor at room temperature.[18] Similarly, Mirzaei *et al.*[19] developed an ambient-temperature hydrogen sensor using a NiO/Nb_2O_5 hybrid composite *via* a hydrothermal method. The NiO/Nb_2O_5 hybrid composite showed a response (1.68%) to 500 ppm H_2 compared to that of pristine Nb_2O_5. Many other approaches have been used to develop metal-oxide heterostructures to improve the sensing performance of devices at room/low temperatures. Over the years, researchers have focused on carbon-based materials for gas-sensing applications. Among these, CNTs stand out for their exceptional electrical and mechanical characteristics and low-temperature operation, making them ideal for the development of highly sensitive and selective sensors.[20,21] However, pristine CNTs lack the necessary selectivity and require surface functionalization to improve their performance. Significant efforts have been made to address this challenge, leading to the discovery that MWCNTs, when combined with various MO_x, significantly improve gas sensing capabilities at room temperatures.[22,23]

Additionally, flexible gas sensors have emerged as a transformative solution in personalized healthcare, offering innovative approaches for remote, non-invasive, and continuous monitoring of health indicators from breath samples without interfering with daily activities. The growing demand for rapid and personalized diagnostic tools has also highlighted the environmental concerns associated with electronic waste from short-lived, conventional silicon-based portable devices. To address this issue, flexible and wearable sensors provide a sustainable and efficient alternative for gas/breath sensing applications. In this study, we developed a cost-effective, flexible gas sensor based on $MWCNTs/Nb_2O_5$ as the sensing material for acetone detection at room temperature. The novelty of this research lies in the preparation of the sensing material, which, to the best of our knowledge, has not previously been explored for detecting breath VOCs. Additionally, the practical effectiveness of the sensor was demonstrated by testing it with various healthy and simulated human breath samples. This approach holds significant potential as a non-invasive monitoring method for managing diabetes.

2. Experimental section

Chemical reagents such as niobium chloride ($NbCl_2$), multi-walled carbon nanotubes (MWCNTs) with a diameter of ∼50 nm, nitric acid (HNO_3), hydrogen peroxide (H_2O_2), acetone and polyethylene terephthalate (PET) substrate (thickness: 100 μm), were procured with AR grade from Sigma Aldrich.

2.1. Preparation of Nb_2O_5 and $MWCNTs/Nb_2O_5$ hybrid sensing materials

Nb_2O_5 NPs were obtained using a hydrothermal method (see Fig. 1). Here, 0.25 g $NbCl_2$ is added to diluted HNO_3 to avoid salt residual, followed by the addition of 5 mL H_2O_2 into the above solution and magnetically stirred for 30 min to obtain a homogenous yellow coloured solution, which indicated the presence of water-soluble $Nb(O_2)^{4-}$ complex. After that, 30 mL of DI water is added to the solution and transferred to a 50 mL autoclave for 22 h at 110 °C. After the reaction, the precipitate was centrifuged at 7000 rpm for 5 min and subsequently washed using acetone and DI water. The obtained slurry is then preheated at 90 °C for 6 h, followed by calcination at 500 °C in a muffle furnace. Similarly, a $MWCNTs/Nb_2O_5$ hybrid was prepared by adding 0.5 wt%, and 1 wt% MWCNTs, just before transferring the solution to the autoclave. Furthermore, all the steps remain the same as used for Nb_2O_5.

2.2. Device fabrication and sensing experiment

A standardized cleaning protocol is implemented to prepare the PET substrate before the deposition of electrodes. The substrate undergoes a sequential cleaning process involving

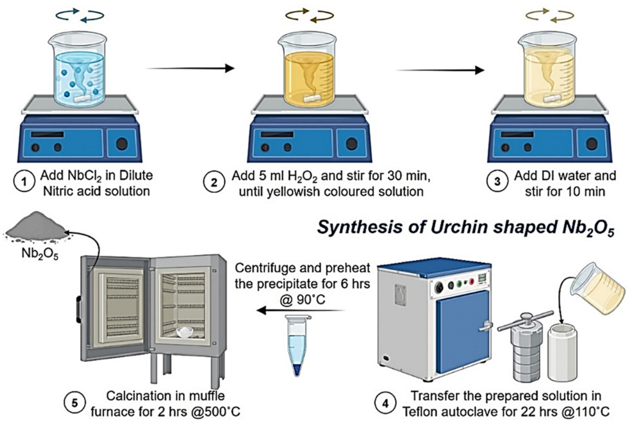

Fig. 1 Schematic representation of the steps involved in the synthesis of Nb_2O_5.

the use of IPA and DI water to remove contaminants. After the cleaning process, the PET film was placed in a thermal evaporation system with a shadow mask, and 30/300 nm Ti/Ag electrodes were deposited. Finally, the electrodes were coated with the sensing materials to fabricate the final devices. An *I–V* curve is recorded in the sensing chamber at ambient temperature to check the development of the prepared device. A voltage of 2 V was applied to these IDEs, which were connected to a Keysight 29018B source meter, to measure the variations in resistance of the prepared sensor under various concentrations of target gas (see Fig. 2). Liquid VOCs were introduced into a sensing chamber using a micro-syringe. The VOCs evaporated rapidly due to the high vapor pressure of the liquid VOC. Moreover, a vacuum pump was employed to eliminate contaminated air from the sensing chamber. The static liquid–gas distribution method was used to determine the target gas concentration based on the formula:[24]

$$C = \frac{22.4 \times \rho \times T \times V_{\mathrm{s}}}{273 \times V \times M_{\mathrm{r}}} \times 1000 \tag{1}$$

where C (in ppm) represents the concentration, ρ (in g cm^{-1}) and M_{r} is the density and molar mass of liquid VOCs, T (in K) is the temperature, and V_{s} (in μL) and V (in L) is the volume of the injected VOCs and volume of the chamber, respectively. Furthermore, the response of the devices was calculated by taking the ratio of the change in resistance before exposure (R_{a}) to the change in resistance after exposure (R_{g}) of the target gas, as expressed in eqn (2).

$$\text{Response }(\%) = \left|\frac{R_{\mathrm{g}} - R_{\mathrm{a}}}{R_{\mathrm{a}}}\right| \times 100\%. \tag{2}$$

To further test the sensor under practical conditions, the real breath samples of healthy volunteers (aged between 20–30 years) were collected in a Tedlar bag, and the experiment was performed with their consent.

2.3. Material characterization

The prepared samples were characterized using various techniques. Field emission scanning electron microscopy (FESEM, Thermo Fisher Scientific) and transmission electron microscopy (TEM, JEOL JEM2100) were employed to examine the morphology and surface details of the samples. The crystallinity was assessed using X-ray diffraction (XRD, Bruker D8 Advanced diffractometer) with Cu K1α radiation (λ = 0.154 nm). Fourier transform infrared spectroscopy (FTIR, Thermo Fisher Scientific) confirmed the phase formation. The elemental composition and total surface area were determined through X-ray photoelectron spectroscopy (XPS, Thermo Fisher Scientific) and Autosorb iQ2 TRX (Quantachrome Instruments), respectively.

2.4. Computational and machine learning (ML) details

The ML code was developed using a Jupyter Notebook (Python v6.4.8) within the Anaconda Navigator environment. The process utilized four essential libraries, including Pandas, NumPy, Scikit-Learn, and SciPy, for data preprocessing, model training, and testing. The programs were run on a computer equipped with an Intel(R) Core(TM) i5-10700 CPU running at 2.90 GHz. The extraction of features such as response time, recovery time, and response (%) from sensor data were carried out to distinguish different analytes, as these features provide useful information. This extracted data was subsequently utilized to train the ML models. For data visualization and dimensionality reduction, t-distributed Stochastic Neighbor Embedding (t-SNE) was used. The supporting document (ESI†) contains a detailed description of the visualization tools and ML algorithms used for the classification and quantification of gases. Furthermore, due to their proven effectiveness in handling small datasets with high accuracy, K-nearest neighbors (KNN), support vector machines (SVM), naive Bayes (NB), and random forest (RF), were selected for gas classification.[25,26] For quantifying gas concentrations, regression algorithms such as linear regression (LR), RF regression (RF-R), KNN regression, and SV regression were used.

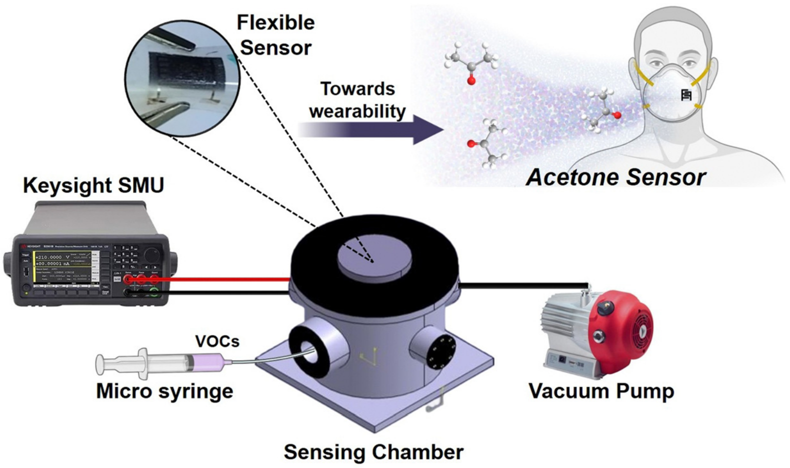

Fig. 2 Schematic view of the gas sensing setup with an inset photograph of the flexible MWCNTs/Nb_2O_5 device.

3. Results and discussion

3.1. Sensing material characterizations

The surface morphology of the hydrothermally synthesized Nb_2O_5 nanoparticles (NPs) is depicted in Fig. 4(A–C). The FESEM image displays interconnected Nb_2O_5 nanostructures with porous spaces in between, indicating the presence of Nb_2O_5 aggregations that may enhance surface roughness. Upon closer examination, the image confirms the successful synthesis of urchin-shaped Nb_2O_5 nanostructures. Furthermore, the possible growth mechanisms of Nb_2O_5 are explained in Fig. 3. Initially, $NbCl_5$ is added to a diluted HNO_3 solution. Subsequently, H_2O_2 was added to the solution to eliminate chloride ions *via* an oxidation–reduction process, which resulted in the appearance of a yellow solution indicating the formation of water-soluble $[Nb(O_2)_4]^{3-}$. Furthermore, the presence of excess H_2O_2 led to the formation of amorphous hierarchical spheres of Nb_2O_5 and $Nb_2O_5{\cdot}nH_2O$. Finally, annealing at 500 °C resulted in the crystallization of Nb_2O_5, which favored pore coalescence due to the crystallization of walls separating mesopores in their structures. Furthermore, when 0.5 wt% and 1 wt% of MWCNTs were incorporated into Nb_2O_5, a mixed morphology of the resulting hybrid was formed.

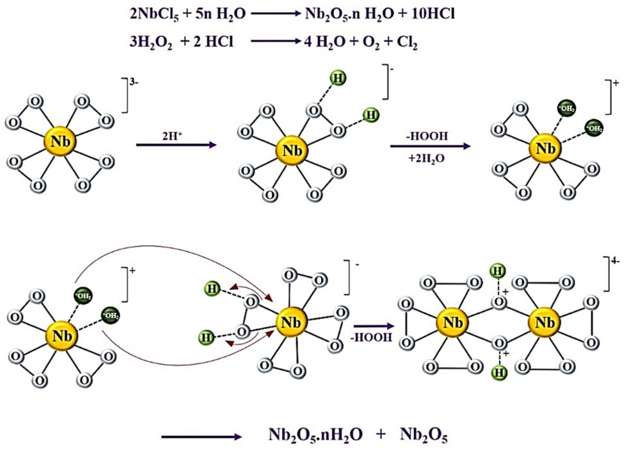

Fig. 3 Possible growth mechanisms of urchin-shaped Nb_2O_5.

As depicted in Fig. 4(D–F), the FESEM images of the 1 wt% MWCNTs/Nb_2O_5 sample exhibit the presence of MWCNTs with a diameter of ∼50 nm, which surround the urchin-shaped Nb_2O_5 NPs. Their unique morphology is expected to offer

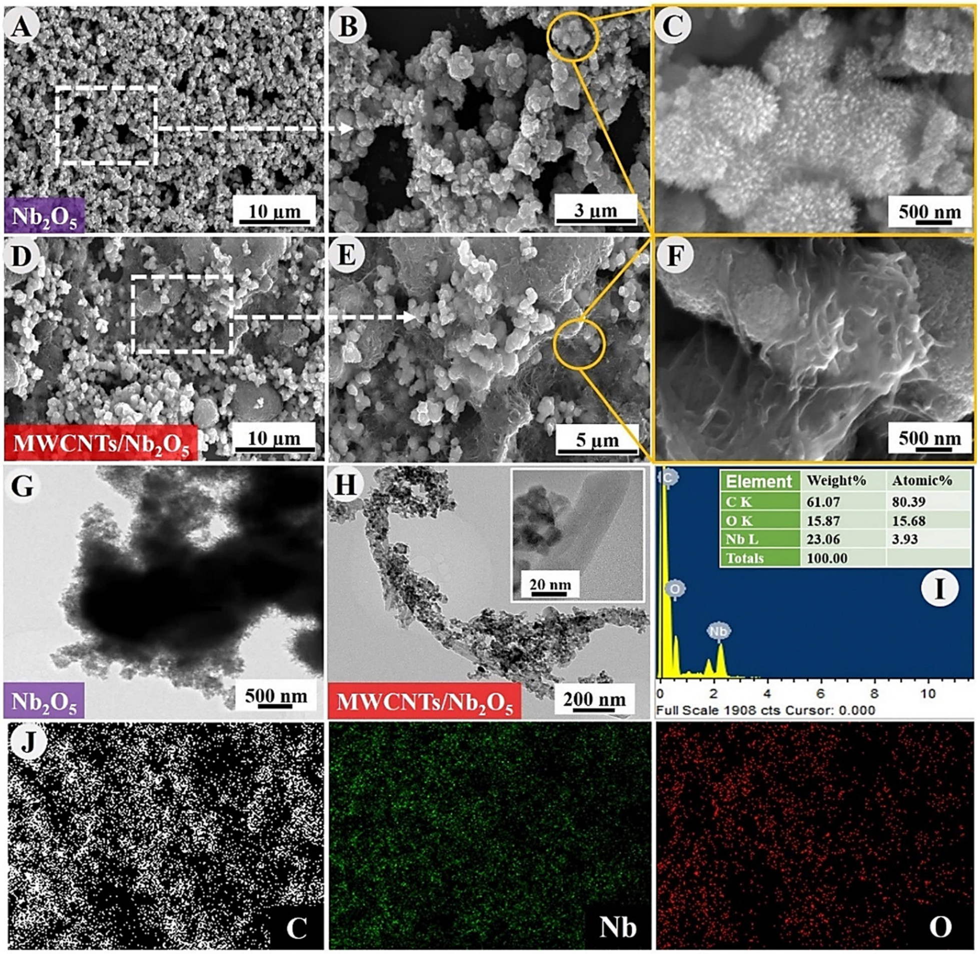

Fig. 4 Low and high magnification FESEM images of (A)–(C) Nb_2O_5 and (D)–(F) 1 wt% MWCNTs/Nb_2O_5, (G) and (H) TEM images of Nb_2O_5 and 1 wt% MWCNTs/Nb_2O_5, and (I) and (J) EDS and elemental mapping of 1 wt% MWCNTs/Nb_2O_5.

significant advantages in gas sensing due to their high surface area and structural characteristics. Furthermore, this arrangement is expected to improve the S/V ratio of the hybrid by increasing the number of adsorption sites for gas molecules during the sensing process. Furthermore, no significant changes in the morphology of the 0.5 wt% MWCNTs/Nb_2O_5 hybrid composite were observed (see Fig. S1, ESI†). Moreover, Fig. 4(G–H) displays the TEM images of Nb_2O_5 NPs and the MWCNT/Nb_2O_5 hybrid. Fig. 4(G) depicts a high dispersion of Nb_2O_5 NPs with a size of ∼15 nm, suggesting a well-organized crystal structure. Additionally, Fig. 4(H) displays a uniform distribution of numerous Nb_2O_5 NPs on the surface of MWCNTs. Fig. S2 (ESI†) depicts the EDS and elemental mapping of pristine Nb_2O_5, which reveals the presence of niobium (Nb) and oxygen (O) elements. The addition of MWCNTs causes the surface of the MWCNTs/Nb_2O_5 hybrid to contain carbon (C), resulting in the presence of C, Nb, and O elements (see Fig. 4(I and J)). The EDS and elemental mapping results confirmed the purity of the prepared hybrid, which aligns with the XRD results.

Furthermore, the crystalline phases of Nb_2O_5 and the MWCNT/Nb_2O_5 hybrid were characterized by XRD (see Fig. 5(a)). The XRD peaks of the Nb_2O_5 NPs calcinated at 500 °C show an orthorhombic structure of Nb_2O_5 NPs with typical peaks at 22.6°, 28.4°, 36.6°, 50.9°, 55.1° and 71.1°. The XRD pattern of the calcined MWCNT/Nb_2O_5 sample exhibited a notable reduction in the amorphous background, suggesting that the crystallinity of the sample increased significantly. This is supported by the appearance of typical peaks corresponding to PDF 96-210-6535 (refer to Fig. S3, ESI†). The synthesis of Nb_2O_5 exhibited a broad absorption spectrum ranging from 200 to 380 nm, as depicted in Fig. 5(b). The absorption peak's starting wavelength was estimated to be ∼280 nm, which corresponds to a band gap energy of 3.2 eV. This finding aligns well with previously reported articles in the literature, highlighting the influence of the synthesis methods.[27,28] With the incorporation of 1 wt% of MWCNTs, the absorption peak displayed a red shift and the adsorption wavelength region was altered, leading to a decrease in the band gap energy (∼2.96 eV) of the MWCNTs/Nb_2O_5 hybrid composite (see Fig. S4, ESI†). Fig. 5(d) displays the FTIR spectra of Nb_2O_5 and the MWCNTs/Nb_2O_5 hybrid. The spectrum of the samples mainly consists of a broad shoulder at 675 cm^{-1}, which is attributed to Nb–O–Nb bridges from distorted octahedral NbO_6.[29] Furthermore, a broad band observed between 850 and 970 cm^{-1} is attributed to the stretching of Nb═O groups.[30] At 1625 cm^{-1}, a peak can be observed that is attributed to water molecules adsorbed on Nb_2O_5's surface. The FTIR spectra of MWCNTs/Nb_2O_5 display similar peaks, along with two additional distinct bands at 1675 and 2983 cm^{-1} corresponding to C═C and C–H stretching vibrations, respectively, from the surface of the nanotubes.[8,31] This finding confirms the development of heterostructure interfaces.

XPS was used to analyze the surface chemistry of the synthesized MWCNTs/Nb_2O_5 hybrid (see Fig. 6(a)). The XPS spectrum of the synthesized hybrid samples shows the presence of Nb, C, and O elements, confirming the high purity of the material. This evidences the decoration of Nb_2O_5 NPs onto the surface of MWCNTs. Fig. 6(b) displays the C 1s XPS spectra of MWCNTs/Nb_2O_5 with three distinct bonds of C–C, C–C, and C═O peaking at 283.7, 284.6, and 290.4 eV, respectively. As compared to the MWCNTs, the binding energies of both the C–O and C═O in the MWCNTs/Nb_2O_5 composite have shifted to lower energies. This could originate from the interaction between Nb_2O_5 NPs and the oxygenated functional groups of the MWCNTs.[32] Furthermore, the chemical interaction between the MWCNTs and Nb_2O_5 NPs is attributed to the construction of Nb–O–C bonds.[33] The O 1s XPS spectrum of the MWCNTs/Nb_2O_5 hybrid shows a peak centered at 530.6 (O–Nb), 531.1 (O═C), and 532.5 eV (O–C), respectively

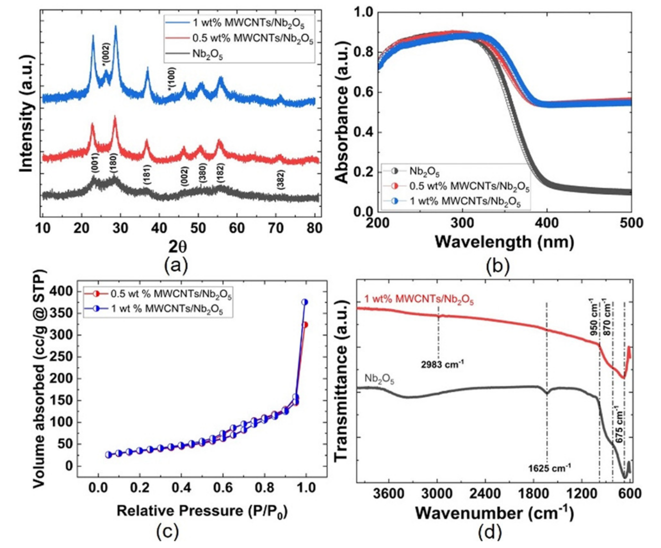

Fig. 5 (a) XRD, (b) UV-Vis, (c) BET, and (d) FTIR spectra of MWCNT/Nb_2O_5 hybrid.

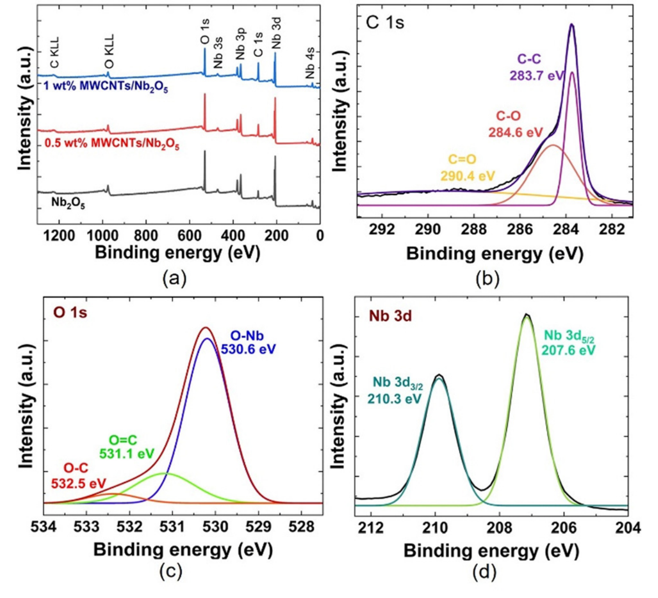

Fig. 6 (a–d) XPS results of Nb_2O_5 and the MWCNT/Nb_2O_5 hybrid.

(see Fig. 6(c)). In addition, Fig. 6(d) shows the Nb 3d spectra with distinct peaks at 207.6 (Nb $3d_{5/2}$) and 210.3 eV (Nb $3d_{5/2}$), respectively, signifying the existence of Nb_2O_5.[34]

4. Gas sensing studies

The *I–V* curves for pristine Nb_2O_5, 0.5 wt%, and 1 wt% MWCNTs/Nb_2O_5 based sensors were measured and recorded, as illustrated in Fig. S5 (ESI†). The results demonstrate that all sensors display a linear relationship, indicative of an ohmic contact. Notably, the pristine Nb_2O_5 sensor shows a lower current at the same applied voltage compared to the MWCNTs/Nb_2O_5 based devices. This suggests that both MWCNTs/Nb_2O_5 devices exhibit increased conductivity, attributed to the synergistic effects of enhanced specific surface area and the formation of heterojunctions upon MWCNT addition. Moreover, the high conductivity promotes the adsorption of atmospheric oxygen species on the surface by capturing electrons, thereby improving the sensing performance, particularly for room-temperature (RT) gas sensing. All the devices demonstrate good stability and reversibility as shown in Fig. 7(a–c), as the response increases rapidly under exposure to different concentrations of gas and returns to its original value upon removal of gas. Furthermore, Fig. 7(a) shows the response (%) of the Nb_2O_5 device for 5–50 ppm acetone gas at RT. The pristine Nb_2O_5 device shows less response to low concentrations of acetone gas at RT. However, at 50 ppm, Nb_2O_5 demonstrated a response of ∼1.5%. Furthermore, the addition of 0.5 wt% MWCNTs in Nb_2O_5 resulted in an improvement in detecting acetone gas at RT (see Fig. 5(b and c)). With changes in the concentration level of acetone gas, the response of the 0.5 wt% MWCNTs/Nb_2O_5 device increased. The sensor showed a response of 1.1% at 5 ppm and gradually increased to ∼3% at 50 ppm. Furthermore, the 1 wt% MWCNTs/Nb_2O_5 devices demonstrated an enhanced response of 1.2% to 3.3% under the exposure of 5 to 50 ppm of acetone gas, respectively.

Fig. 7(f) illustrates the comparative response (%) plot of all devices. The results highlight the superior response of the 1 wt% MWCNTs/Nb_2O_5 device at each acetone gas concentration. Furthermore, the device shows ∼1.18 × (118% higher response by proportion) and ∼2.1 × (210% higher response by proportion) after loading the 1 wt% MWCNTs to a pristine Nb_2O_5 device. The impact of adding MWCNTs to Nb_2O_5 can be partly explained by considering their work functions: Nb_2O_5 has a work function of ∼4.29 eV,[35] while MWCNTs have a work function of ∼4.95 eV.[36] This difference in work function causes electrons to transfer from Nb_2O_5 to MWCNTs at their interface. Additionally, the high surface area of MWCNTs increases their adsorption capacity, thereby enhancing the adsorption ability of the Nb_2O_5 surface when they are combined. As a result, as the gas concentration increases, the response shows an increasing trend. Additionally, Fig. 7(d and e) displays the response and recovery times of all devices for acetone gas. The response times to 5 ppm and 50 ppm acetone are nearly the same, *i.e.*, 66 s and 70 s, respectively. However, the recovery time shows an opposite trend compared to the response time. This can be explained by the dynamic balance between gas adsorption and desorption. At low concentrations, gas adsorption dominates, taking longer to reach equilibrium, thus resulting in a longer response time. Conversely, at higher concentrations, equilibrium is achieved more quickly, leading to a shorter response time. In our study, we found that the sensor's response time is nearly the same for both 5 ppm and 50 ppm. During the recovery process at room temperature, gas desorption primarily

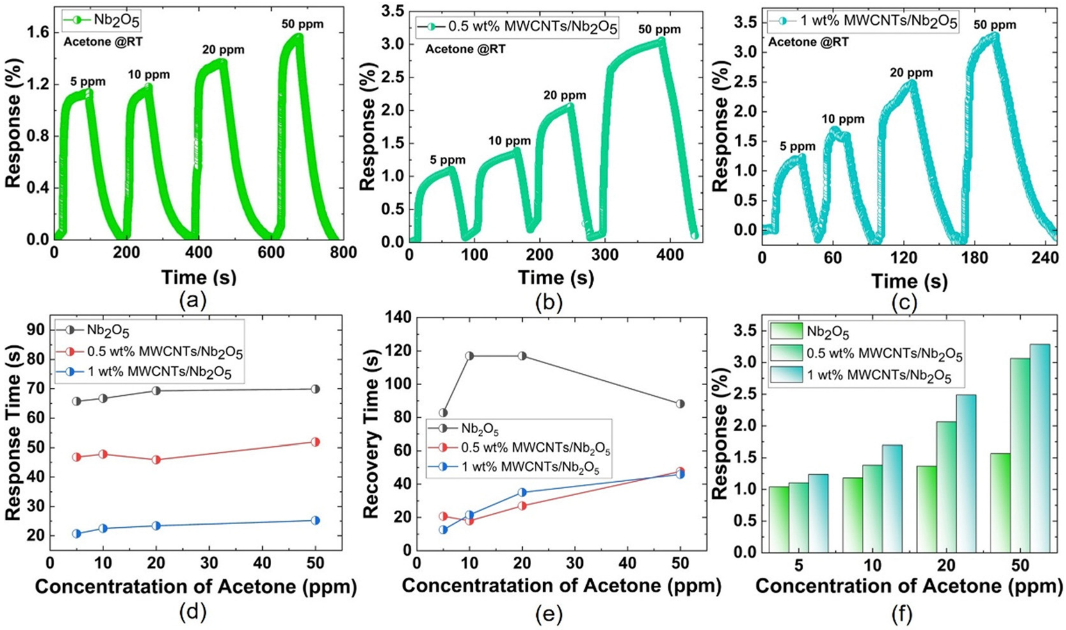

Fig. 7 Graphs depicting the time–dependent response (%) for (a) Nb_2O_5, (b) 0.5 wt%, and (c) 1 wt% MWCNT/Nb_2O_5 hybrid, (d)–(f) a comparative response/recovery time graph and response (%) for Nb_2O_5 and (0.5 wt% and 1 wt%) MWCNT/Nb_2O_5 hybrids.

depends on diffusion,[37] resulting in a generally longer recovery time. Additionally, the response process produces water, which affects gas desorption (see chemical reactions in Fig. 12). Typically, additional heating is required to provide the gas with enough energy for desorption. In our experiments, no heating was applied during the recovery process, so the recovery time is slightly longer than the response time. The results further demonstrate the superiority of the 1 wt% MWCNTs/Nb_2O_5 device, showcasing the fastest response and recovery times compared to other devices. Fig. 8(a) illustrates the response and recovery times of the device at 50 ppm acetone, which are 25 s and 46 s, respectively.

To evaluate the practicality of the prepared flexible devices, the performance of the 1 wt% MWCNTs/Nb_2O_5 sensor was examined through tests for repeatability, sensitivity, selectivity, and stability. Fig. 8(b) depicts the consistency of the sensor when subjected to 50 ppm of acetone gas, as demonstrated in the repeatability test. The results showed that the device's response remained consistent throughout a three-cycle test, indicating stability and potential for practical use. Furthermore, sensitivity was determined by the change in response for every 1 ppm variation in the target gas concentration, represented by the slope of the linear regression line in Fig. 8(c), which is calculated to be 0.0828%/ppm. Using this slope, the sensor's limit of detection (LOD) can be derived with the formula: LOD = 3 × (rms/slope).[38] The root mean square (rms) deviation, computed from the fifth-order polynomial fit of the baseline, was found to be 0.00913 for the 1 wt% MWCNTs/Nb_2O_5 sensor (see Fig. 8(d)). This results in an LOD of $\sim$330 ppb. In actual use, room-temperature flexible devices must have the ability to differentiate between various gases. The selectivity of the 1 wt% MWCNTs/Nb_2O_5 sensor was subsequently assessed and depicted in Fig. 8(e). The relative response (%) for 50 ppm ethanol, methanol, and toluene was found to be lower as compared to acetone. Furthermore, the sensor was subjected to a stability test that spanned across a 20-day duration, revealing that the sensor exhibited negligible variation in response (see Fig. 8(f)). These results indicate that the device is well suited for applications in environmental, domestic, and healthcare settings.

4.1. Visualization, classification, and predictions of analytes through ML algorithms

Before using ML algorithms, feature extraction is the first stage in preprocessing any sensor signal. A total of 192 data points (4 analytes, 4 concentrations, 3 features (response time, recovery time, and response (%)), 4 cycles = 4 × 4 × 3 × 4) were extracted from the 1 wt% MWCNTs/Nb_2O_5 sensor for all analytes, namely acetone, ethanol, methanol, and toluene (see Fig. 9(a–c)). One effective method to identify sensor data with the highest prediction accuracy is to visualize the data in lower dimensions. A t-SNE method was used to visualize the collected data points. The distinct cluster formation in t-SNE demonstrated that no instances of overlap exist between the clusters, indicating that the data is classifiable (see Fig. 9(d)). Furthermore, this indicates that the selected features can be used for regression and classification of gases.

Four classifier algorithms, specifically SVM, RF, NB, and KNN, were used in conjunction with the k-fold cross-validation technique to optimize the utilization of the existing data and

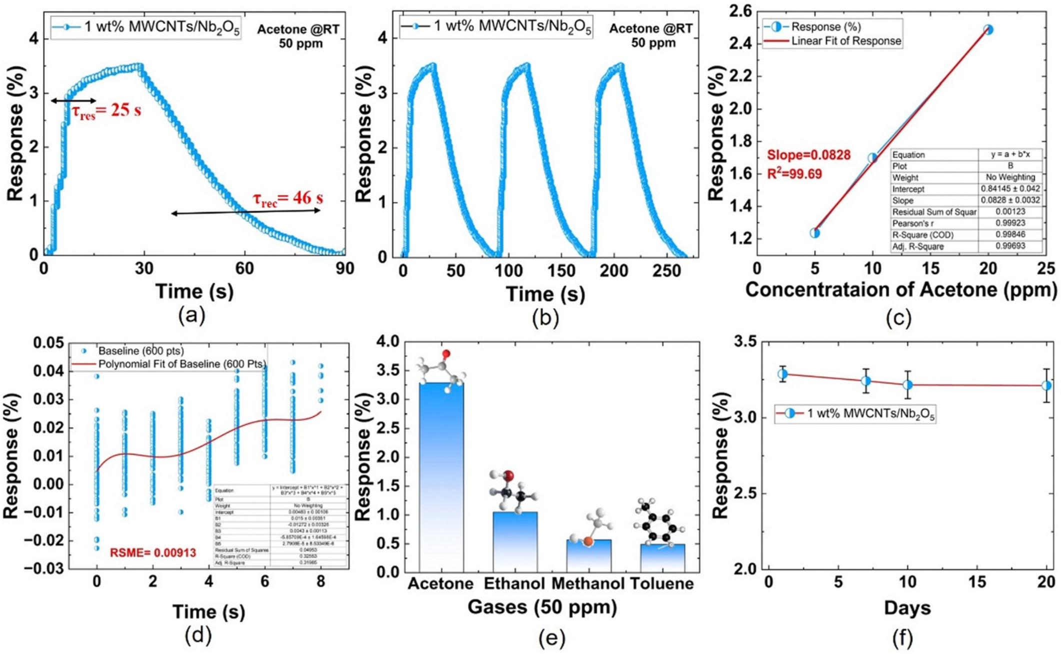

Fig. 8 (a) Response of 1 wt% MWCNTs/Nb_2O_5 to 50 ppm acetone concentration at RT, (b) three-cycle repeatability test conducted at 50 ppm acetone, (c) and (d) linear regression analysis for sensitivity calculation based on response, and 5th order polynomial fit of the base, (e) selectivity, and (f) stability results.

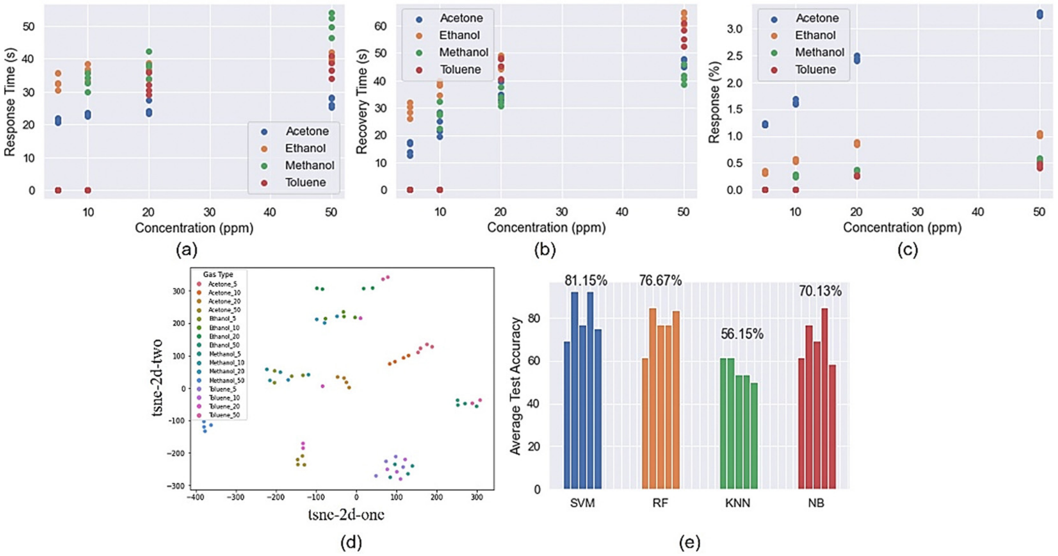

Fig. 9 (a)–(c) Extracted feature of the sensor for four different gases, namely: acetone, ethanol, methanol, and toluene, (d) t-SNE plots of extracted data points, and (e) five-fold cross validation test accuracies of the SVM, RF, KNN, and NB algorithms.

determine the classification algorithm parameters for the target analyte. *K*-fold cross-validation involves randomly partitioning the original data into *k* subsamples. Out of these subsamples, k^{-1} groups are utilized for training, while the remaining group is used for validation. The distribution was iterated *k* times, resulting in the mean accuracy of all iterations. The classification accuracy for the test data in each split of the observed fivefold CV is shown in Fig. 9(e). The average test accuracies for SVM, RF, KNN, and NB are 81.15%, 76.67%, 56.15%, and 70.13%, respectively. SVM is a maximum margin classifier, *i.e.*, it has an optimal margin gap between separate hyperplanes, resulting in the production of expected test accuracies. Whereas KNN resulted in lower accuracy as there is no learning involved, unlike in the case of SVM and RF.

For the practical implementation of any desired application, qualitative gas detection alone would not be sufficient. To determine the precise concentration of the gases of interest, regression methods were used following the accurate classification of the gases. To conduct a regression analysis, the entire dataset was segregated into two separate subsets: a training set comprising 60% of the data, and a testing set consisting of 40% of the data, which corresponded to each analyte. The algorithms showed excellent performance in accurately estimating the concentrations of all target analytes. Specifically, the mean absolute error (MAE) values for acetone, ethanol, methanol, and toluene using LR were 27.42, 20.40, 11.86, and 22.85, respectively. Similarly, SVR accurately modelled the datasets, yielding MAE values of 82.13, 39.09, 194.99, and 40.98, respectively. The RF regressor demonstrated a strong fit and accurate prediction, as evidenced by the MAE values of 2.78, 1.87, 17.88, and 23.90 for acetone, ethanol, methanol, and toluene, respectively. Lastly, the KNN regressor resulted in MAE values of 24.60, 9.13, 19.84, and 62.70 for acetone, ethanol, methanol, and toluene, respectively. Fig. 10 illustrates the comparison between the actual data (denoted by dashed diagonal lines) and the predicted data (denoted by symbols) for all analytes. The regression models exhibit a high level of accuracy with minimal error at lower concentrations. However, as the concentrations increase, there are deviations from the expected values, indicating a lack of accuracy in the fit.

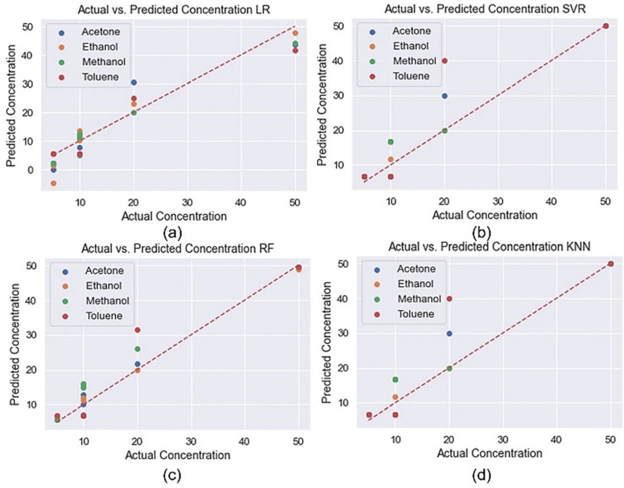

Fig. 10 (a)–(d) Gases are quantitatively analyzed using LR, RF, SVM, and KNN regression.

We conducted further experiments to examine the potential of a 1 wt% MWCNTs/Nb$_2$O$_5$ device for breath analysis, which was attached to a commercially available N95 mask (see inset of Fig. 12). In our study, a breath sample of a healthy volunteer was collected in a 1L Tedlar bag and further mixed with acetone (5 ppm) to simulate the breath of diabetic patients (see Fig. 11(a)). Fig. 11(b and c) illustrates the response (%) of the sensor in the presence of both simulated diabetic and healthy

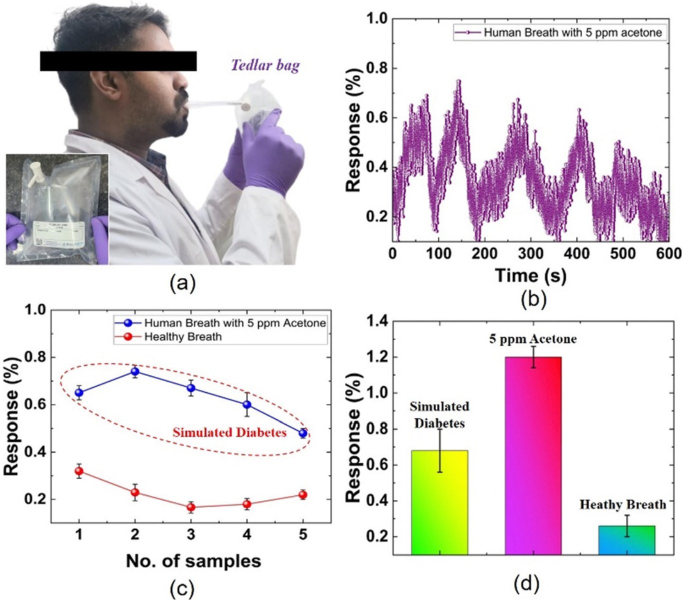

Fig. 11 (a) Collection of the breath of healthy volunteers in a Tedlar bag; (b) response of the device under the conditions of simulated diabetes, where 5 ppm acetone was injected into the collected breath samples from healthy volunteers; (c) response curve of the device for different volunteer samples, distinguishing between healthy and simulated diabetic breath; (d) comparison of the device responses when exposed to simulated diabetic breath, 5 ppm acetone, and breath from healthy volunteers.

breath environments. Furthermore, the sensor underwent a comparative analysis under exposure to simulated diabetes, 5 ppm acetone, and healthy breath samples. The results depicted in Fig. 11(d) indicate that the sensor's response toward simulated diabetes is less pronounced than its response to pristine acetone (5 ppm); however, it remains significantly higher compared to its response to healthy breath. This capability suggests the potential to distinguish between healthy and diabetic individuals. Therefore, the 1 wt% MWCNTs/Nb_2O_5 sensor exhibits promising prospects for detecting biomarkers in future applications for respiratory diagnosis. Moreover, the comparative analysis of previously developed flexible devices with room temperature acetone gas detection is shown in Table 1.

The primary sensing of Nb_2O_5 relies on the changes in resistance resulting from the adsorption and desorption processes, which are caused by the interactions between adsorbed O^{2-} and the target gases on the surface of the sensing layer.[7] In particular, the sensing performance of the MWCNTs/Nb_2O_5 hybrid has shown significant improvements over pristine Nb_2O_5. This could be due to the following factors; firstly, when the MWCNTs/Nb_2O_5 based sensor is exposed to air, oxygen molecules capture electrons from the conduction band of the hybrid material, transforming into O^{2-} species at RT.[8] These chemisorbed O^{2-} species form a depletion layer on the MWCNTs/Nb_2O_5 surface, affecting the baseline resistance in air and reacting with the acetone introduced later.[43] At RT, the interaction between acetone and the adsorbed O^{2-} releases electrons, which are rapidly transferred through the conductive channels formed by the Nb_2O_5 and MWCNT interface.[44] This promotes further reactions with the acetone, thereby enhancing the sensor's response. The involved chemical interaction between acetone and absorbed O^{2-} is presented in Fig. 12. Secondly, the improved sensing characteristics of the MWCNTs/Nb_2O_5 hybrid are attributed to enhanced resistance modulation due to the p-type doping of MWCNTs and the formation of a p–n heterojunction between MWCNTs and Nb_2O_5. The work function of Nb_2O_5 is ~4.29 eV,[35,45] while that of MWCNTs is ~4.9 eV.[36] This difference in work function

Table 1 Comparative analysis of acetone-based sensors operating at RT

Material	Temp. (°C)	Response (%)	τ_{res} (s)	τ_{rec} (s)	LOD
Ag@CNT[39]	RT	~1.64 (100 ppm)	13	10	50 ppm
NiO–WO_3[40]	300	4.4 (200 ppm)	51	59	5 ppm
rGO-Se[41]	135	3.2 (100 ppm)	13	10	25 ppm
$ZnFe_2O_4$-GQDs[42]	RT	3.2 (100 ppm)	11	4	5 ppm
MWCNTs/Nb_2O_5 (this work)	RT	~3.3 (50 ppm)	25	46	330 ppb

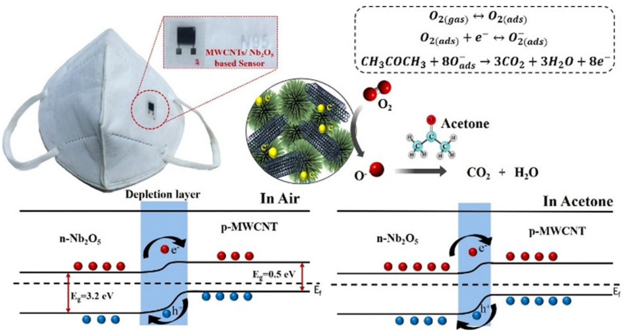

Fig. 12 Sensing mechanisms of the MWCNTs/Nb_2O_5 based sensor with the inset photograph of an N95 mask attached to a flexible acetone sensor.

drives electron transfer from Nb_2O_5 to MWCNTs at their interface. As a result, there is an accumulation of charge carriers at the interface, which enhances the overall electrical conductivity of the composite material. Finally, there is a substantial morphological transformation. For instance, the urchin-shaped Nb_2O_5, when evenly coated on the exterior of the MWCNTs, improves the specific surface area to 121 $m^2 g^{-1}$ (as confirmed by the BET as shown in Fig. 5(c)) and the conductivity of the hybrid material. Moreover, the MWCNTs/Nb_2O_5 exhibit an improved capacity to absorb O_2^- ions and provide abundant active sites for interaction with acetone gas. This enhancement is attributed to their increased surface area and minimized particle aggregation.

5. Conclusions

This study demonstrated the fabrication of a flexible MWCNTs/Nb_2O_5 based breath sensor for detecting acetone at ambient temperature. The results of the structural and morphological experiments indicated the successful synthesis of a sensing material, which was then coated onto a flexible PET substrate to fabricate the breath sensing devices. Furthermore, the prepared sensor with 1 wt% MWCNTs/Nb_2O_5 demonstrated fast response/recovery times of 26/45 s, respectively, as well as reliable stability, selectivity, and detection limit of 330 ppb for acetone gas. Furthermore, characteristic features were extracted from the breath sensor. Various ML algorithms were used to visualize, classify, and predict the tested analyte with good quantifications. In addition, the sensor demonstrated its ability to effectively distinguish between healthy and simulated diabetic breath samples. The presented results indicate the significant potential of this breath sensor for detecting acetone in both environmental and human breath samples.

Data availability

The data supporting this article have been included as part of the ESI.†

Conflicts of interest

There are no conflicts to declare.

Acknowledgements

The author, Gulshan Verma (G.V.), is pleased to acknowledge the Ministry of Education (MoE), India, and IIT Jodhpur for a financial assistantship. Additionally, the authors express sincere thanks to all volunteers who participated in the study. Informed consent was obtained from each participant. Pranay Ranjan (P.R.) would like to thank SERB for SRG (Grant No. SRG/2022/000192), SEED grant no. I/SEED/PRJ/20220044, IDRP IIT Jodhpur and QIC IIT Jodhpur for its Support.

References

1 C. Li, P. G. Choi, K. Kim and Y. Masuda, *Sens. Actuators, B*, 2022, **367**, 132143.
2 G. Verma and A. Gupta, *J. Micromech. Microeng.*, 2022, **32**, 094002.
3 D. Zhang, A. Liu, H. Chang and B. Xia, *RSC Adv.*, 2014, **5**, 3016–3022.
4 M. Benamara, P. Rivero-Antúnez, H. Dahman, M. Essid, S. Bouzidi, M. Debliquy, D. Lahem, V. Morales-Flórez, L. Esquivias, J. P. B. Silva and L. El Mir, *J. Sol-Gel Sci. Technol.*, 2023, **108**, 13–27.
5 J. Li, L. Li, Q. Chen, W. Zhu and J. Zhang, *J. Mater. Chem. C*, 2022, **10**, 860–869.
6 P. Španěl, K. Dryahina, A. Rejšková, T. W. E. Chippendale and D. Smith, *Physiol. Meas.*, 2011, **32**, N23.
7 A. Gupta and G. Verma, *Nanostructured Gas Sensors: Fundamentals, Devices, and Applications*, Jenny Stanford Publishing, New York, 2023.
8 G. Verma, V. Pandey, M. Islam, M. Kumar and A. Gupta, *J. Micromech. Microeng.*, 2023, **33**, 095003.
9 G. Verma, V. Kishnani, R. K. Pippara, A. Yadav, P. S. Chauhan and A. Gupta, *Sens. Actuators, A*, 2021, **332**, 113111.
10 X. Xiao, G. Dong, C. Xu, H. He, H. Qi, Z. Fan and J. Shao, *Appl. Surf. Sci.*, 2008, **255**, 2192–2195.
11 A. Le Viet, R. Jose, M. V. Reddy, B. V. R. Chowdari and S. Ramakrishna, *J. Phys. Chem. C*, 2010, **114**, 21795–21800.
12 S. Ramakrishna, A. Le Viet, M. V. Reddy, R. Jose and B. V. R. Chowdari, *J. Phys. Chem. C*, 2010, **114**, 664–671.
13 H. Zhang, Y. Wang, D. Yang, Y. Li, H. Liu, P. Liu, B. J. Wood and H. Zhao, *Adv. Mater.*, 2012, **24**, 1598–1603.
14 R. Ab Kadir, R. A. Rani, M. M. Y. A. Alsaif, J. Z. Ou, W. Wlodarski, A. P. O'Mullane and K. Kalantar-Zadeh, *ACS Appl. Mater. Interfaces*, 2015, **7**, 4751–4758.
15 M. H. Habibi and R. Mokhtari, *J. Inorg. Organomet. Polym. Mater.*, 2012, **22**, 158–165.
16 H. Wen, Z. Liu, J. Wang, Q. Yang, Y. Li and J. Yu, *Appl. Surf. Sci.*, 2011, **257**, 10084–10088.
17 I. Zhitomirsky, *Mater. Lett.*, 1998, **35**, 188–193.
18 T. Hyodo, H. Shibata, Y. Shimizu and M. Egashira, *Sens. Actuators, B*, 2009, **142**, 97–104.
19 A. Mirzaei, G. J. Sun, J. K. Lee, C. Lee, S. Choi and H. W. Kim, *Ceram. Int.*, 2017, **43**, 5247–5254.
20 G. Verma, N. Sheshkar, C. Pandey and A. Gupta, *J. Polym. Res.*, 2022, **29**, 1–26.
21 G. Verma and A. Gupta, *J. Mater. Nanosci.*, 2022, **9**, 3–12.
22 G. Verma, A. Gokarna, H. Kadiri, K. Nomenyo, G. Lerondel and A. Gupta, *ACS Sens.*, 2023, **8**, 3320–3337.
23 S. G. Bachhav, D. R. Patil, S. G. Bachhav and D. R. Patil, *J. Mater. Sci. Chem. Eng.*, 2015, **3**, 30–44.
24 L. Malepe, T. D. Ndinteh, P. Ndungu and M. A. Mamo, *Nanoscale Adv.*, 2023, **5**, 1956–1969.
25 S. Acharyya, B. Jana, S. Nag, G. Saha and P. K. Guha, *Sens. Actuators, B*, 2020, **321**, 128484.
26 S. Kulkarni, B. N. Bharath and R. Ghosh, *IEEE Sens. J.*, 2023, **23**, 10293–10300.

27 T. Sreethawong, S. Ngamsinlapasathian and S. Yoshikawa, *Mater. Lett.*, 2012, **78**, 135–138.

28 T. Fuchigami and K. I. Kakimoto, *J. Mater. Res.*, 2017, **32**, 3326–3332.

29 O. F. Lopes, E. C. Paris and C. Ribeiro, *Appl. Catal., B*, 2014, **144**, 800–808.

30 F. Idrees, R. Dillert, D. Bahnemann, F. K. Butt and M. Tahir, *Catalysis*, 2019, **9**, 169.

31 F. A. Hezam, A. Rajeh, O. Nur and M. A. Mustafa, *Phys. B*, 2020, **596**, 412389.

32 M. Y. Song, N. R. Kim, H. J. Yoon, S. Y. Cho, H. Jin and Y. S. Yun, *ACS Appl. Mater. Interfaces*, 2017, **9**(3), 2267, DOI: **10.1021/acsami.6b11444**.

33 J. Yu and B. Cheng, *J. Mater. Chem. A*, 2014, **2**, 3407–3416.

34 Z. Dai, H. Dai, Y. Zhou, D. Liu, G. Duan, W. Cai and Y. Li, *Adv. Mater. Interfaces*, 2015, **2**, 1500167.

35 Y. T. Huang, R. Cheng, P. Zhai, H. Lee, Y. H. Chang and S. P. Feng, *Electrochim. Acta*, 2017, **236**, 131–139.

36 M. Narjinary, P. Rana, A. Sen and M. Pal, *Mater. Des.*, 2017, **115**, 158–164.

37 F. Meng, H. Zheng, Y. Chang, Y. Zhao, M. Li, C. Wang, Y. Sun and J. Liu, *IEEE Trans. Nanotechnol.*, 2018, **17**, 212–219.

38 G. Verma, H. Kadiri, A. Gokarna, S. Kumar, M. Kumar, G. Lerondel and A. Gupta, *Sens. Actuators, B*, 2025, **422**, 136621.

39 S.-J. Young, Y.-H. Liu, Z.-D. Lin, K. Ahmed, M. N. I. Shiblee, S. Romanuik, P. K. Sekhar, T. Thundat, L. Nagahara, S. Arya, R. Ahmed, H. Furukawa and A. Khosla, *J. Electrochem. Soc.*, 2020, **167**, 167519.

40 S. Choi, J. K. Lee, W. S. Lee, C. Lee and W. I. Lee, *J. Korean Phys. Soc.*, 2017, **71**, 487–493.

41 A. Hussain Shar, M. Nazim Lakhan, K. Tawfik Alali, J. Liu, M. Ahmed, A. Hussain Shah and J. Wang, *Chem. Phys. Lett.*, 2020, **755**, 137797.

42 X. Chu, P. Dai, S. Liang, A. Bhattacharya, Y. Dong and M. Epifani, *Phys. E*, 2019, **106**, 326–333.

43 W. Shao, J. Lu, Z. Zheng, R. Liu, X. Wang, Z. Zhao, Y. Lu, L. Zhu and Z. Ye, *ACS Appl. Mater. Interfaces*, 2023, **15**, 4315–4328.

44 C. Li, K. Kim, T. Fuchigami, T. Asaka, K. Ichi Kakimoto and Y. Masuda, *Sens. Actuators, B*, 2023, **393**, 134144.

45 P. V. Tyagi, M. Doleans, B. Hannah, R. Afanador, C. McMahan, S. Stewart, J. Mammosser, M. Howell, J. Saunders, B. Degraff and S. H. Kim, *Appl. Surf. Sci.*, 2016, **369**, 29–35.